

# MRQy: An Open-Source Tool for Quality Control of MR Imaging Data

Amir Reza Sadri<sup>1</sup>, Andrew Janowczyk<sup>1</sup>, Ren Zhou<sup>1</sup>, Ruchika Verma<sup>1</sup>,  
Niha Beig<sup>1</sup>, Jacob Antunes<sup>1</sup>, Anant Madabhushi<sup>1,2</sup>, Pallavi Tiwari<sup>1</sup>,  
and Satish E Viswanath<sup>1</sup>

<sup>1</sup> Department of Biomedical Engineering, Case Western Reserve University, Cleveland, OH 44106, USA

<sup>2</sup> Louis Stokes Cleveland VA Medical Center, Cleveland, OH 44106, USA

Version typeset August 18, 2020  
Corresponding author: sev21@case.edu

## Abstract

**Purpose:** We sought to develop a quantitative tool to quickly determine relative differences in MRI volumes both within and between large MR imaging cohorts (such as available in The Cancer Imaging Archive (TCIA)), in order to help determine the generalizability of radiomics and machine learning schemes to unseen datasets. The tool is intended to help quantify presence of (a) site- or scanner-specific variations in image resolution, field-of-view, or image contrast, or (b) imaging artifacts such as noise, motion, inhomogeneity, ringing, or aliasing; which can adversely affect relative image quality between data cohorts.

**Methods:** We present MRQy, a new open-source quality control tool to (a) interrogate MRI cohorts for site- or equipment-based differences, and (b) quantify the impact of MRI artifacts on relative image quality; to help determine how to correct for these variations prior to model development. MRQy extracts a series of quality measures (e.g. noise ratios, variation metrics, entropy and energy criteria) and MR image metadata (e.g. voxel resolution, image dimensions) for subsequent interrogation via a specialized HTML5 based front-end designed for real-time filtering and trend visualization.

**Results:** MRQy was used to evaluate (a) n=133 brain MRIs from TCIA (7 sites), and (b) n=104 rectal MRIs (3 local sites). MRQy measures revealed significant site-specific variations in both cohorts, indicating potential batch effects. Marked differences in specific MRQy measures were also able to identify outlier MRI datasets that needed to be corrected for common MR imaging artifacts.

**Conclusions:** MRQy is designed to be a standalone, unsupervised tool that can be efficiently run on a standard desktop computer. It has been made freely accessible at <http://github.com/ccipd/MRQy> for wider community use and feedback.

# Contents

<b>I. Introduction</b>	<b>1</b>
<b>II. Materials and Methods</b>	<b>4</b>
II.A. Input . . . . .	4
II.B. Backend Processing . . . . .	4
II.B.1. Foreground Detection . . . . .	4
II.B.2. Information Extraction . . . . .	6
II.C. Front-end Visualization . . . . .	6
II.C.1. Tables . . . . .	7
II.C.2. Charts . . . . .	8
II.C.3. Scatter Plots . . . . .	8
II.D. Experimental Design . . . . .	9
II.D.1. TCGA-GBM cohort . . . . .	9
II.D.2. In-house rectal cancer cohort . . . . .	9
II.D.3. Evaluation . . . . .	10
<b>III. Results</b>	<b>10</b>
III.A. Assessment of TCGA-GBM datasets for batch effects and imaging artifacts .	10
III.B. Evaluation of multi-site rectal cancer cohort via MRQy . . . . .	11
III.C. Quantitative evaluation of batch effects before and after processing . . . . .	14
<b>IV. Discussion</b>	<b>15</b>
<b>V. Conclusions</b>	<b>17</b>
<b>Supplemental Materials</b>	<b>19</b>
<b>References</b>	<b>21</b>

## 1. Introduction

The development of public repositories such as The Cancer Imaging Archive (TCIA)<sup>1,2</sup> have enabled significant advances in machine and deep learning approaches via radiographic imaging for a variety of oncological applications<sup>3,4</sup>. With over 2500 MR imaging scans for 26 unique anatomic sites obtained from different centers and using a variety of scanner equipment, a key aspect to utilizing TCIA cohorts for reliable model development and optimization of computational imaging tools<sup>5</sup> is to curate datasets with minimal to no artifacts; implying they are relatively homogeneous in appearance<sup>6</sup>. Quantitative assessment of variations or artifacts known to exist in MRI data<sup>7</sup> can also provide *a priori* cues regarding the generalizability of computational imaging models to unseen datasets, by helping identify:

- *Site- and scanner-specific variations* which can cause poor reproducibility of machine learning models between cohorts and sites<sup>8,9</sup>. Beyond just differences in image acquisition parameters such as echo and repetition times, there may also be systematic occurrences of technical variations (e.g. voxel resolution or fields-of-view) in subsets of a cohort i.e. *batch effects*<sup>10</sup>. These are exemplified by distinctive variations in image and voxel dimensions both within as well as across 7 distinct sites within The Cancer Genome Atlas Glioblastoma Multiforme (TCGA-GBM) collection<sup>11</sup> in Figure 1.
- *Presence of imaging artifacts* which adversely affect the relative quality of clinical MR imaging scans within a cohort and significantly degrade model performance<sup>12</sup>. Issues such as magnetic field inhomogeneity, aliasing, motion, ringing, or noise<sup>13,14</sup> can cause individual datasets to deviate significantly from the remainder of the cohort; and need to be identified and corrected prior to analysis<sup>15,16</sup>.

Evaluating variations and relative image quality between cohorts is thus critical to determine whether a radiomics or deep learning model that was trained on one cohort will perform reproducibly on a different cohort. Identification of artifacts in individual MRI datasets (known as *image quality assessment*) may be performed by experts, however, visual inspection is known to lack sensitivity to subtle variations between MR images<sup>17</sup>. Subjective quality ratings are also not precise enough to rigorously curate MRI cohorts<sup>18</sup> due to inter-rater variability. Additionally, it may be infeasible to laboriously and manually assess the quality of individual imaging datasets in large public repositories such as TCIA. This underscores the

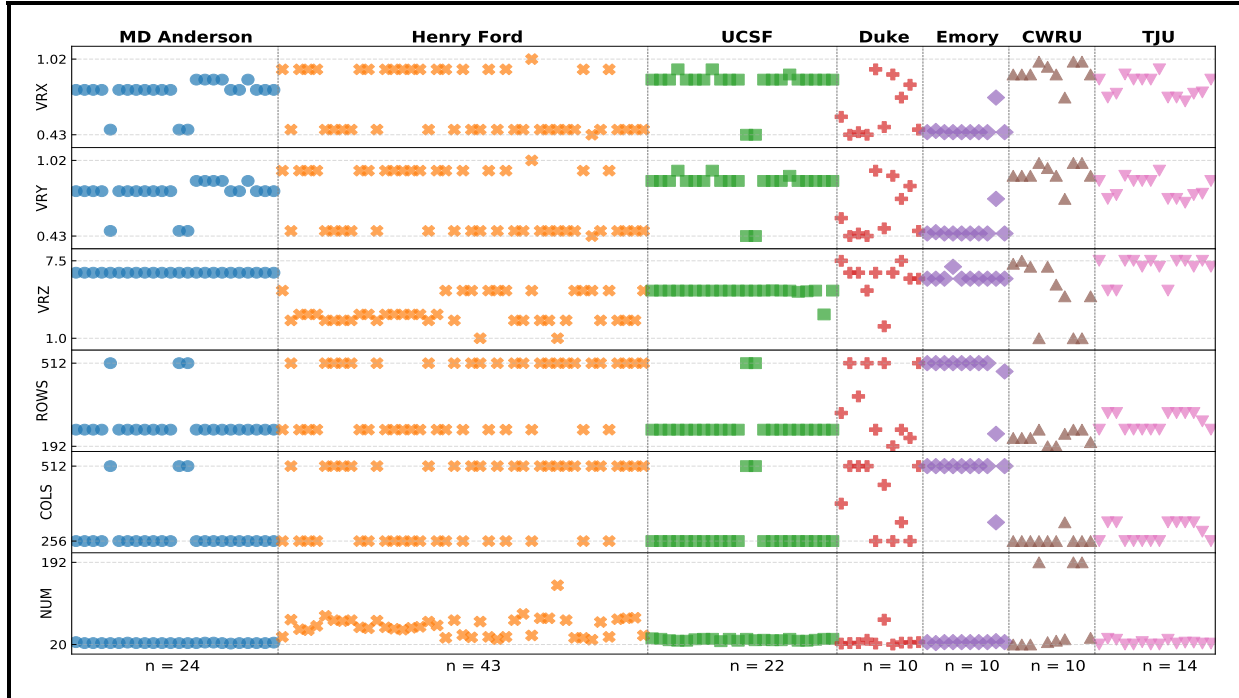


Figure 1: Variations in MRI scan metadata illustrating batch effects within the TCGA-GBM cohort across 133 post-contrast T1-weighted MRI datasets curated from 7 different sites (in different colors) where each point corresponds to a unique subject.  $VRX$ ,  $VRY$ , and  $VRZ$  correspond to voxel resolutions in-plane ( $x$ ,  $y$ ) and through-plane ( $z$ ) respectively.  $ROWS$  and  $COLS$  represent in-plane scan size and the  $NUM$  is the number of images in each volume. All information was directly extracted from DICOM metadata of each MRI dataset, as downloaded from TCIA.

need for automated *quality control (QC)* tools for MRI scans, defined in this context as quantitative approaches that can be used to identify ranges of acceptability for MR imaging datasets<sup>63</sup>. Importantly, QC allows a user to quickly identify when a quality measurement falls outside a user-specified range or tolerance, so that an appropriate corrective action can be taken (for specific datasets or the cohort as a whole)<sup>64</sup>. Such QC tools also need to work with minimal to no user intervention while enabling reliable curation of artifact-free and congruent data cohorts for further computational analysis and model development.

Efforts towards automated quality control of MRI datasets has led to development of different Image Quality Metrics (IQMs)<sup>19,20</sup> as well as a Quality Assessment Protocol (QAP)<sup>21</sup>. However, most studies evaluating IQMs (e.g. noise ratios, energy ratios, entropy values) have focused on supervised prediction of whether a brain MRI should be *accepted* or *excluded*, as defined by experts<sup>20,22,23</sup>. IQMs have also been implemented in tools such as MRIQC<sup>18</sup>

Table 1: Feature comparison of open-source MRI quality control tools

Attribute	MRIQC <sup>18</sup>	Qoala-T <sup>25</sup>	LABQA2GO <sup>26</sup>	MRIQC-WebAPI <sup>24</sup>	Mindcontrol <sup>55</sup>	VisualQC <sup>56</sup>	MRQy
Body part	brain	brain	brain	brain	brain	brain	all
Supporting raw data (.dcm,.nii)	✓	✓	✓	✓	✓	✓	✓
Supporting processed data (.mha)	✗	✗	✗	✗	✗	✓	✓
Supporting modular plugins	✗	✗	✗	✗	✓	✓	✓
Supporting phantom data	✗	✗	✓	✗	✗	✗	✓
Interactive user interface	✓	✗	✗	✓	✓	✓	✓
Batch effects identification	✓	✗	✗	✓	✗	✓	✓
Measurements	14	185	-	14	3+9	-	13+10

which is a supervised quality classification tool for predicting expert quality ratings for brain MRIs. More recently, MRIQC was adapted to use a web-application program interface to facilitate efficient interactions with expert quality ratings and quality annotations<sup>24</sup>. Other quality control and prediction tools for brain MRIs include the FreeSurfer-specific Qoala-T<sup>25</sup> and LABQA2GO<sup>26</sup>; where the latter outputs an HTML report of image quality measures. However, as summarized in Table 1, none of these tools<sup>18,24,25,26,55,56</sup> are readily generalizable to MRIs of body regions other than the brain, or provide an interactive front-end that can be used to easily interrogate quality issues and batch effects that may be present in large-scale imaging cohorts.

In this work, we present a technical overview of MRQy, a new open-source quality control tool for MR imaging data. MRQy builds on the HistoQC Python framework<sup>27</sup> and has been specialized for analyzing large-scale MRI cohorts through the following modules: (i) automatic foreground detection for any MR image from any body region, from which it will (ii) extract a series of imaging-specific metadata and quality measures<sup>21</sup> generalized to work with any structural MR sequence, in order to (iii) compute representations that capture relevant MR image quality trends in a data cohort. These are presented within a specialized HTML5-based front-end which can be used to: (a) interrogate trends in per-site and per-scanner variations in a multi-site setting, (b) identify which specific image artifacts are present in which MRI scans in a data cohort, and (c) curate together cohorts of MRI datasets which are consistent and of sufficient image quality for computational model development. We will demonstrate the usage of MRQy via a representative publicly available brain MRI cohort from TCIA as well as an in-house multi-site rectal MRI cohort. MRQy works in an unsupervised standalone setting, runs efficiently on a standard computer, and has a modular design to allow for easy incorporation of additional algorithms and metrics as plugins in the future.

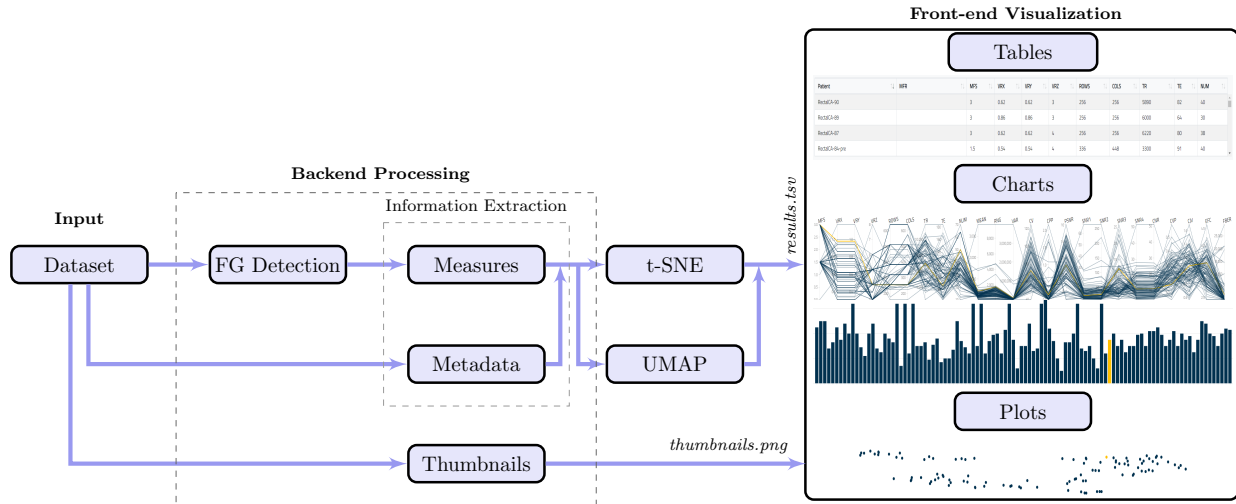


Figure 2: Schematic for overall MRQy workflow and major components.

## II. Materials and Methods

The major components of the MRQy tool are illustrated in Figure 2, which can be sub-divided into three specific modules: Input, Backend Processing, and Front-end Visualization.

### II.A. Input

To ensure MRQy supported popular file formats for storing radiographic data (e.g. *.dcm*, *.nii*, *.mha*, and *.ima*), the packages `medpy` and `pydicom` libraries<sup>28</sup> were used. MRQy iteratively parses either a single directory input (containing files) or resources through a directory of directories, in order to read in the image volume as well as parse image metadata.

### II.B. Backend Processing

#### II.B.1. Foreground Detection

As the MRI volume input to MRQy could be acquired from any body region, it is crucial to first identify the primary area within the volume from which quality measures are calculated. An in-house image processing algorithm was developed to efficiently and automatically extract and separate the background (outside the body) from the foreground (primary region of interest), as illustrated in Figure 3.

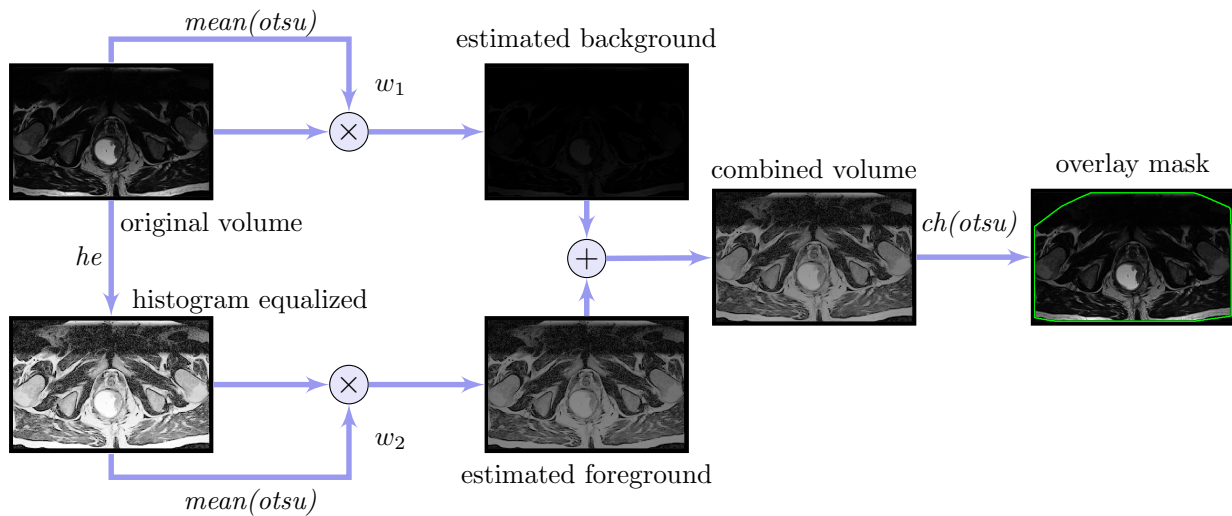


Figure 3: Schematic of the foreground detection algorithm.

Otsu thresholding is typically proposed as an efficient approach to quickly identify both these regions in an MRI volume, but common shadowing/shading artifacts that are present in MRI volumes are known to significantly affect its performance<sup>29</sup>. By contrast, histogram equalization could help articulate details in the MRI volume even with shading or shadow artifacts, but is known to also intensify the appearance of noise<sup>30</sup>. In order to take advantage of both methods simultaneously, a weighted combination of the original MRI volume and its histogram equalized version were used as an input to Otsu thresholding. The weights were defined automatically to ensure a completely unsupervised method. A convex hull operation was then used to enclose the foreground based on the mask output from Otsu thresholding. While this algorithm was designed primarily for scans with one primary foreground region, it has been generalized to be able to detect and return multiple individual foreground objects that may be present in an MR image (e.g. axial slices over both legs<sup>34</sup>). The Supplementary Materials section has additional details on settings that can be specified by the end-user in this regard.

These steps were implemented using the `scikit-image` python package<sup>31</sup>. Representative results of foreground detection are illustrated in Figure 4 for MRIs of the brain and the rectum to demonstrate the generalizability of the algorithm across different body regions, including in MR images with minimal background (i.e. “zoomed” acquisitions or those with sufficient phase oversampling, see Figure 4(e)).

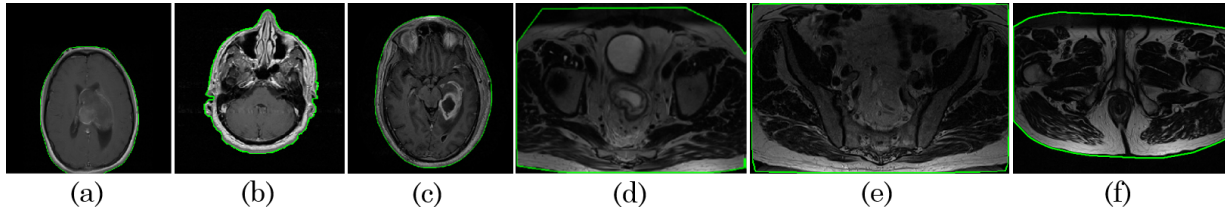


Figure 4: Representative foreground detection results with the foreground outlined in green for representative (a), (b), (c) brain MRI sections, (d), (e), (f) rectal MRI sections. Region outside the green outline is considered background. Note accurate delineation of outer boundary despite visually apparent shadowing and noise artifacts on all MRIs, regardless of body region being imaged.

### II.B.2. Information Extraction

Two major types of information were extracted from each MRI volume, broadly categorized as *Metadata* and *Measurements* (summarized in Table 2). These were saved into a tab-separated file for further analysis.

- *Metadata*: This information that was directly extracted from file headers, such as voxel resolution or MRI volume dimensions (summarized in Table 2, rows 1-10).
- *Measurements*: These were selected from a survey of the medical imaging literature<sup>18,21,35,36</sup> for detecting specific artifacts in MRI scans. This list included statistical measures (e.g. range, variance, %CV) as well as second-order statistics and filter-based measures (e.g. contrast per pixel (CPP), entropy focus criterion (EFC), signal-to-noise ratios of different regions). Table 2 (rows 13-23) summarizes the measures extracted by MRQy, their mathematical formulation, and what type of artifact they were each intended to quantify.

## II.C. Front-end Visualization

The interactive user-interface of MRQy was built as a locally hosted HTML5/Javascript file (compatible with popular web browsers such as Google Chrome, Firefox, or Chromium); specifically designed for real-time analytics, data filtering, and interactive visualization by the end-user. The goal was to allow end-users to easily investigate trends in site or scanner variations within an MRI cohort, as well as identify those scans that require additional



Table 2: Summary table of metadata and quality measures extracted within MRQy

Type	Metric	Description*
Metadata	MFR	manufacturer name from the file header
	MFS	magnetic field strength from the file header
	VRX	voxel resolution in x plane
	VRY	voxel resolution in y plane
	VRZ	voxel resolution in z plane
	ROWS	rows value of the volume
	COLS	columns value of the volume
	TR	repetition time value of the volume
	TE	echo time value of the volume
	NUM	number of slice images in each volume
Measurements	MEAN	mean of the foreground ( $m_1 = \mu_F = \frac{1}{MN} \sum_{i,j} F(i,j)$ )
	RNG	range of the foreground ( $m_2 = \max(F) - \min(F)$ )
	VAR	variance of the foreground ( $m_3 = \sigma_F^2$ )
	CV	coefficient of variation of the foreground for shadowing and inhomogeneity artifacts <sup>48</sup> ( $m_4 = \frac{\sigma_F}{\mu_F}$ )
	CPP	contrast per pixel <sup>35</sup> : mean of the foreground filtered by a $3 \times 3$ 2D Laplacian kernel for shadowing artifacts ( $m_5 = \text{mean}(\text{conv2}(F, f_1))$ , $f_1 = \frac{1}{8} \begin{bmatrix} -1 & -1 & -1 \\ -1 & 8 & -1 \\ -1 & -1 & -1 \end{bmatrix}$ )
	PSNR	peak signal to noise ratio of the foreground <sup>49</sup> ( $m_6 = 10 \log \frac{\max^2(F)}{\text{MSE}(F, f_2)}$ , $f_2$ is a $5 \times 5$ median filter)
	SNR1	foreground standard deviation (SD) divided by background SD <sup>14</sup> ( $m_7 = \frac{\sigma_F}{\sigma_B}$ )
	SNR2	mean of the foreground patch divided by background SD <sup>18</sup> . ( $m_8 = \frac{\mu_{FP}}{\sigma_B}$ )
	SNR3	foreground patch SD divided by the centered foreground patch SD ( $m_9 = \frac{\mu_{FP}}{\sigma_{FP - \mu_{FP}}}$ )
	SNR4	mean of the foreground patch divided by mean of the background patch ( $m_{10} = \frac{\mu_{FP}}{\sigma_{BP}}$ )
	CNR	contrast to noise ratio for shadowing and noise artifacts <sup>14</sup> : mean of the foreground and background patches difference divided by background patch SD ( $m_{11} = \frac{\mu_{FP} - \mu_{BP}}{\sigma_{BP}}$ )
	CVP	coefficient of variation of the foreground patch for shading artifacts: foreground patch SD divided by foreground patch mean ( $m_{12} = \frac{\sigma_{FP}}{\mu_{FP}}$ )
	CJV	coefficient of joint variation between the foreground and background for aliasing and inhomogeneity artifacts <sup>41</sup> ( $m_{13} = \frac{\sigma_F + \sigma_B}{ \mu_F - \mu_B }$ )
	EFC	entropy focus criterion for motion artifacts <sup>18</sup> : $m_{14} = \frac{NM}{\sqrt{NM}} \log \frac{E}{\sqrt{NM}}$ , $E = - \sum_{i,j} \frac{F(i,j)}{F_{\max}} \ln \frac{F(i,j)}{F_{\max}}$ , $F_{\max} = \sqrt{\sum_{i,j} F^2(i,j)}$
	FBER	foreground-background energy ratio for ringing artifacts <sup>50</sup> : ( $m_{15} = \frac{\text{median}( F ^2)}{\text{median}( B ^2)}$ )

\* All the computed measurements (numbered  $m_1 - m_{15}$ ) are average values over the entire volume, which calculated for every single slice separately. Variables  $M, N, F, B, FP, BP$  stand for slice width size, slice height size, foreground image intensity values, background image intensity values, foreground patch, and background patch respectively. Operators  $\mu, \sigma, \sigma^2$ , median stand for mean, standard deviation (SD), and variance measures respectively. Foreground and background patches are random  $5 \times 5$  square patches of the foreground and background images respectively. Measurements SNR1-SNR4 are all signal to noise ratio with different definitions.

processing due to the presence of artifacts. The MRQy interface splits into 3 major sections, all of which are inter-connected. Any individual section can also be disabled or re-enabled by the end-user to provide a fully customizable interface.

### II.C.1. Tables

Extracted metadata and measures appear in separate tables within the interface. Each table has sortable columns to easily view outliers in numeric values. Any incomplete metadata values are displayed as “NA” (as well as being ignored in subsequent visualizations). In-

formation can easily be copied out of the tables, which are also fully configurable including allowing for removal of specific subjects or specific columns.

### II.C.2. Charts

- Parallel Cordinate (PC): This is a multivariate visualization tool which has been shown to be effective for understanding trends within multi-variate datasets<sup>37</sup>. For each MRI volume, a polyline is plotted (i.e. an unbroken line segment) which connected vertices of patient measurements on the parallel axes; i.e the vertex position on each axis corresponds to the value of the point for that specific metadata field or measure. The PC chart offered a visual approach to check variations in each measure as they related to the rest of the cohort as well as aided in the identification of outliers.
- Bar: A single bar is plotted per MRI volume for a selected variable (either metadata or measures). This provides an alternative approach to evaluating individual variables, where outliers would be markedly taller or shorter than the remainder of the cohort.

### II.C.3. Scatter Plots

To examine how the MRI volumes in a cohort relate to one another as well as to examine site- or scanner-specific trends, 2 different “embeddings” were computed based on the t-SNE<sup>38</sup> and UMAP<sup>39</sup> algorithms within the Python backend. Both these algorithms take as an input all 23 measures for each patient and output a 2-dimensional embedding space (visualized as a scatter plot) where similarities between patients are preserved. While t-SNE yields a relatively robust representation of overall cohort structure, UMAP additionally provides a topological data structure that has been shown to be more accurate than t-SNE in some settings<sup>39</sup>. t-SNE was implemented using the `sklearn.manifold` Python package<sup>28</sup> with default parameters (e.g. `n_components = 2`, `perplexity = 30`, `random_state = 0`), while UMAP utilized the `umap-learn` Python package<sup>28</sup> in the backend with default parameters (`n_components = 1`, `n_neighbors= 15`, `min_dist= 0.1`, `metric = 'euclidean'`).

## II.D. Experimental Design

### II.D.1. TCGA-GBM cohort

TCGA-GBM is the largest available dataset of brain MRI data from the Cancer Imaging Archive (TCIA)<sup>11</sup>, and comprises scans from  $n=259$  subjects. This study was limited to subjects for whom a post-contrast T1-weighted MR image in the axial plane was available, resulting in a cohort of  $n=133$  T1-POST MRI scans accrued from 7 different sites (also visualized in Figure 1). As these MRI scans were acquired under different environmental conditions and using different scanner equipment and imaging protocols, this cohort includes typical data variations and image artifacts that may be observed in a TCIA dataset<sup>40</sup>. All 133 T1-POST studies were downloaded as DICOM files from TCIA.

In addition to the original cohort (as downloaded from TCIA), a processed version of the TCGA-GBM cohort was obtained from a publicly accessible release by Bakas et al<sup>40</sup>. Briefly, processed MR volumes had been made available as NIFTI files after undergoing the following steps: (1) re-orientation to the left-posterior-superior coordinate system, (2) co-registration to the T1w anatomical template of SRI24 Multi-Channel Normal Adult Human Brain Atlas via affine registration<sup>53</sup>, (3) resampling to  $1\text{ mm}^3$  voxel resolution<sup>54</sup>, (4) skull-stripping<sup>57</sup>, (5) de-noising using a low-level image processing smoothing filter<sup>58</sup>, and intensity standardization to an image distribution template<sup>61</sup>.

### II.D.2. In-house rectal cancer cohort

This retrospectively curated dataset comprised 104 patients accrued from three different institutions including the Cleveland Clinic (CC,  $n=60$ ), University Hospitals (UH,  $n=35$ ), and the Cleveland Veterans Affairs (VA,  $n = 9$ ) (further details available in [ 42]). For all patients, a T2-weighted turbo spin-echo MRI sequence had been acquired from patients diagnosed with rectal adenocarcinoma. While all scans were anonymized DICOM files, they had been acquired with different sequence parameters and using different scanner equipment; thus making the cohort an exemplar of a retrospectively accrued multi-site cohort.

Both the original scans as well as processed scans in this cohort were utilized, where in the latter case all MRI datasets had undergone the following sequence of operations: (1) linear resampling to a consistent voxel resolution of  $0.781 \times 0.781 \times 4.0\text{ mm}$ , (2) N4ITK bias

field correction<sup>59</sup>, and (3) image intensity normalization with respect to a muscle region<sup>60,62</sup>. The processed images were available as MHA files.

### II.D.3. Evaluation

The MRQy front-end was used to assess each of the two cohorts for batch effects as well as image quality artifacts. In order to determine how congruent and consistent the cohorts were as a result of processing, the output of MRQy was compared between the original unprocessed and the processed scans (i.e. after applying artifact correction and normalization operations). All analysis was conducted using Python 3.7.4 for backend processing and Google Chrome 80.0.3987.149 for interacting with the front-end on a PC with Intel(R) Core(TM) i7 CPU 930 (3.60 GHz), 32 GB RAM, and a 64 bit Windows 10 operating system.

The performance of MRQy measures in identifying batch effects in each cohort without any *a priori* knowledge was evaluated via consensus clustering<sup>51</sup> of all 23 measures using the `ConsensusClusterPlus` package in R<sup>52</sup>. Hierarchical consensus clustering (with  $k = 7$  for TCGA-GBM and  $k = 3$  for the rectal cohort) was performed using Pearson distance and 1000 iterations, including 80% random dataset resampling between iterations. The result was visualized as a consensus cluster heatmap where the shading indicated the frequency with which a pair of patients was clustered together. Cluster overlap accuracy was then computed by first identifying which cluster corresponded to which site (based on precision/recall values) and then calculating what fraction of the datasets from each site had been correctly clustered together in consensus clustering.

## III. Results

### III.A. Assessment of TCGA-GBM datasets for batch effects and imaging artifacts

Analysis via MRQy took 93.5 minutes to process all 133 datasets in the original TCGA-GBM cohort ( $\approx 42$ s/dataset) and 101.6 minutes ( $\approx 46$ s/dataset) for the processed cohort. Quality control of the TCGA-GBM cohort via the MRQy front-end interface (Figure 5(a)) reveals the following:

- Imaging artifact detection: The PC chart of the CJV measure (Figure 5(b), unprocessed cohort mean  $CJV=1.30 \pm 0.06$ ) shows the presence of a distinct outlier (highlighted in orange + orange arrow,  $CJV=1.64$ ). Further visualizing representative images (Figure 5(c)) from this dataset depicts a distinct shading artifact compared to a different dataset from the cohort ((Figure 5(c), cyan arrow in PC chart,  $CJV=1.2$ ). This is the specific image artifact that the CJV measure is designed to quantify<sup>41</sup>, which indicates this dataset requires bias correction or intensity normalization prior to computational analysis.
- Correction of image artifacts after processing: Examining the PC chart of the CJV measure of processed scans (Figure 5(f), cohort mean  $CJV=0.605 \pm 0.05$ ) reveals no distinct outliers (the highlighted dataset from Figure 5(b) has  $CJV=0.604$  after processing). Figure 5(g) and (h) depict processed images corresponding to those in Figure 5(c) and (d) respectively. This suggests that the processing steps have accounted for the intensity artifacts previously identified, as reflected in the CJV measure.
- Batch effect detection: Significant site-specific variations are seen to be present in the embedding scatter plot overlaid with different colored symbols for each site ((Figure 5(e)). Each of the 7 sites appear as a distinct cluster, suggesting batch effects that need to be corrected for prior to model development.
- Correction of batch effects after processing: The embedding scatter plot reveals no distinctive clusters corresponding to any site, where the colored symbols in Figure 5(i) fall within a single merged cluster; suggesting that the processing steps may have successfully accounted for site-specific variations.

### III.B. Evaluation of multi-site rectal cancer cohort via MRQy

Analysis via MRQy took 51.8 minutes to process all 104 original datasets in rectal cohort ( $\approx 30s/dataset$ ) and 60.28 minutes ( $\approx 35s/dataset$ ) for the processed cohort. Using the MRQy front-end (Figure 6(a) for raw dataset and Figure 6(d) for processed data) for quality control revealed the following:

- Imaging artifact detection before and after processing: The bar chart of PSNR values

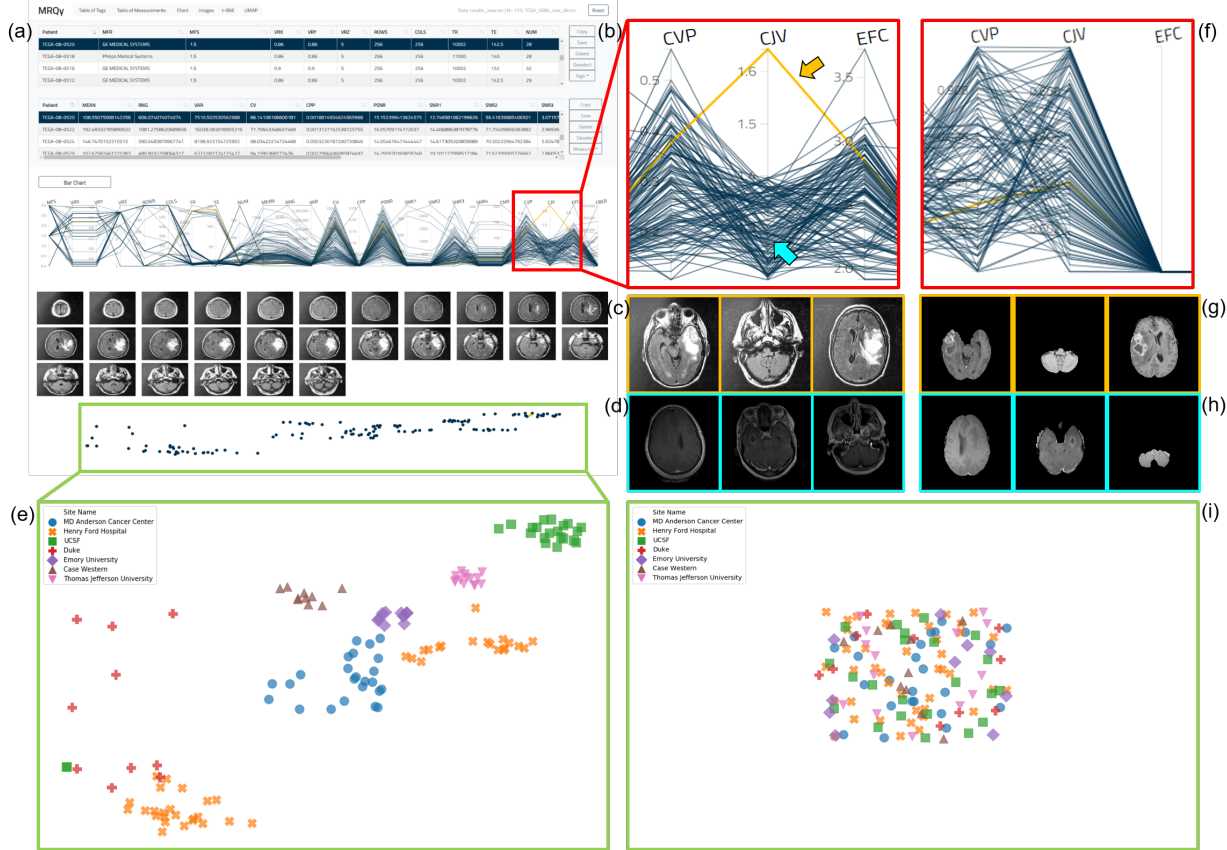


Figure 5: (a) MRQy front-end interface for interrogating TCGA-GBM cohort before processing. (b) Outlier dataset identified on PC chart for the CJV measure found to exhibit shading artifact on (c) representative images, especially when compared to (d) a different dataset. (e) Scatter plot revealing presence of site-specific batch effects in this cohort before processing (colored symbols corresponding to different sites appear in site-specific clusters). (f) corresponds to (b) after data processing. (g) Processed images corresponding to (c). (h) Processed images corresponding to (d). (i) Scatter plot of the processed data fall within a single merged cluster.

(Figure 6(b)), unprocessed cohort mean PSNR= $11.17 \pm 2.38$ ) helps quickly identify a specific dataset with very poor PSNR (indicated via orange arrow, PSNR=0.2). PSNR thus appears to accurately characterize noise artifacts in MR images as designed<sup>18</sup>, suggesting this dataset requires denoising prior to analysis. In the processed cohort, the PSNR value for this dataset (Figure 6(e), orange arrow, PSNR=18.4) is markedly higher as well as appears more consistent with the remainder of the cohort (processed cohort mean PSNR= $17.94 \pm 1.42$ ).

- Batch effect detection before and after processing: Marked batch effects are seen to be

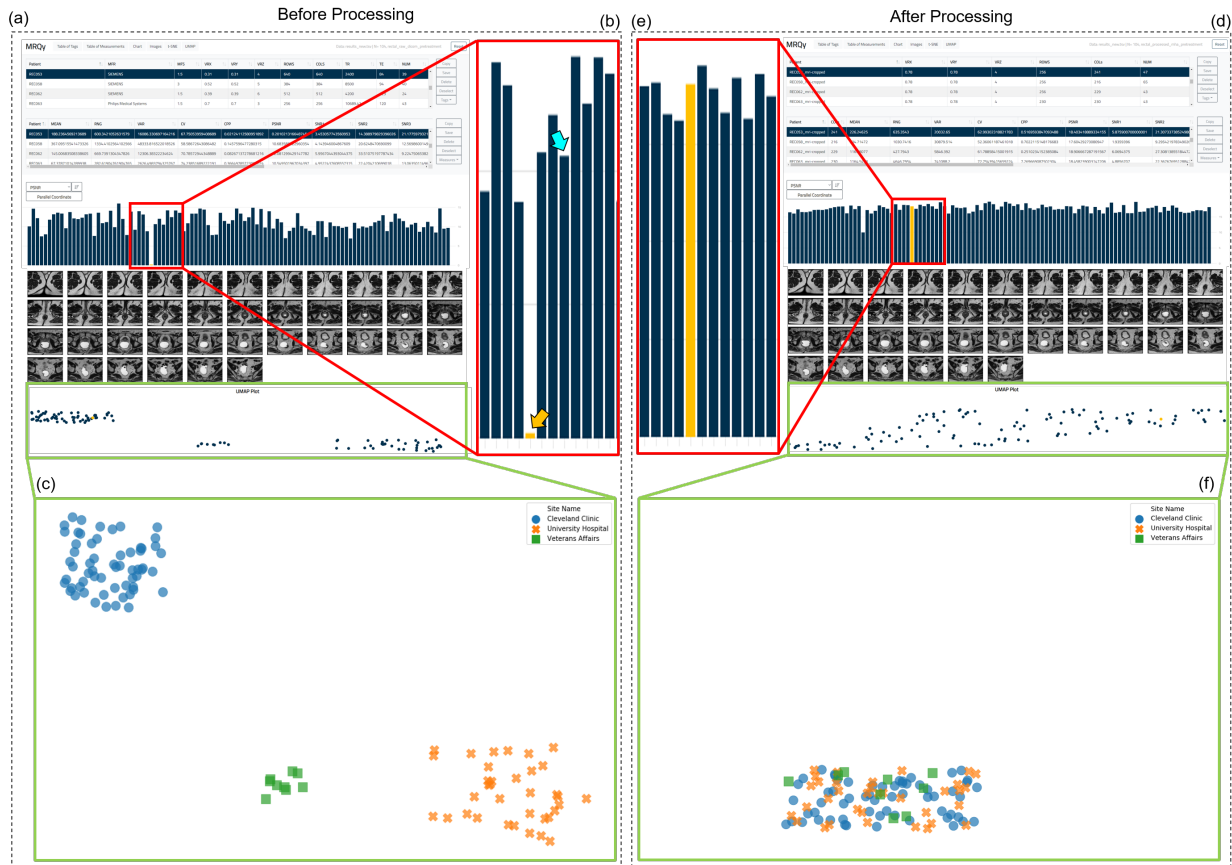


Figure 6: (a) MRQy front-end interface for interrogating rectal cohort before processing. (b) Outlier dataset identified on the bar chart for the PSNR measure found to exhibit subtle noise artifacts. (c) Scatter plot reveals presence of site-specific clusters in this cohort before processing (colored symbols corresponding to different sites appear in site-specific clusters). (d) MRQy front-end interface showing results using processed data. (e) Improved PSNR value of dataset highlighted in (b) after processing, also more consistent with remainder of cohort. (f) Scatter plot a single merged cluster for the cohort, suggesting batch effects and site-specific variations may have been accounted for.

present in the scatter plot in Figure 6(e) as each of the colored symbols (corresponding to different sites in the unprocessed cohort) appear in distinct clusters. By contrast, the scatter plot of the processed cohort in Figure 6(f) reveals a single merged cluster suggesting that site-specific differences have been accounted for.

**III.C. Quantitative evaluation of batch effects before and after processing**

Figure 7(a) and (b) visualizes the clustergrams for each cohort (based on unprocessed data) obtained via consensus clustering of the 23 measures. For the TCGA-GBM cohort, the cluster overlap accuracy of MRQy measures with respect to each of the 7 sites is 87.5%, 86.4%, 90%, 93%, 90%, 60%, and 92.9% respectively. Similarly, MRQy measures are found to cluster each of the 3 sites in the rectal cohort with an overlap accuracy of 91%, 82.8%, and 88.9%, respectively. The strong co-clustering of datasets from the same site as well as relatively high clustering accuracy of datasets within site-specific groupings are suggestive of batch effects in both cohorts.

Corresponding clustergrams for the processed datasets are shown in Figure 7(c) (for TCGA-GBM cohort) and Figure 7(d) (for rectal cohort). After processing, the cluster overlap accuracy of MRQy measures in the TCGA-GBM cohort for each of the 7 sites reduced to 16.67%, 2.33%, 4.55%, 70%, 10%, 20%, and 7.14% respectively. Similarly, the cluster overlap accuracy for each of the 3 sites in the rectal cancer cohort is 1.67%, 0%, and 88.89%, respectively. This suggests that none of the clusters identified via MRQy measures are associated with any specific site after processing, in either cohort.



## IV. DISCUSSION

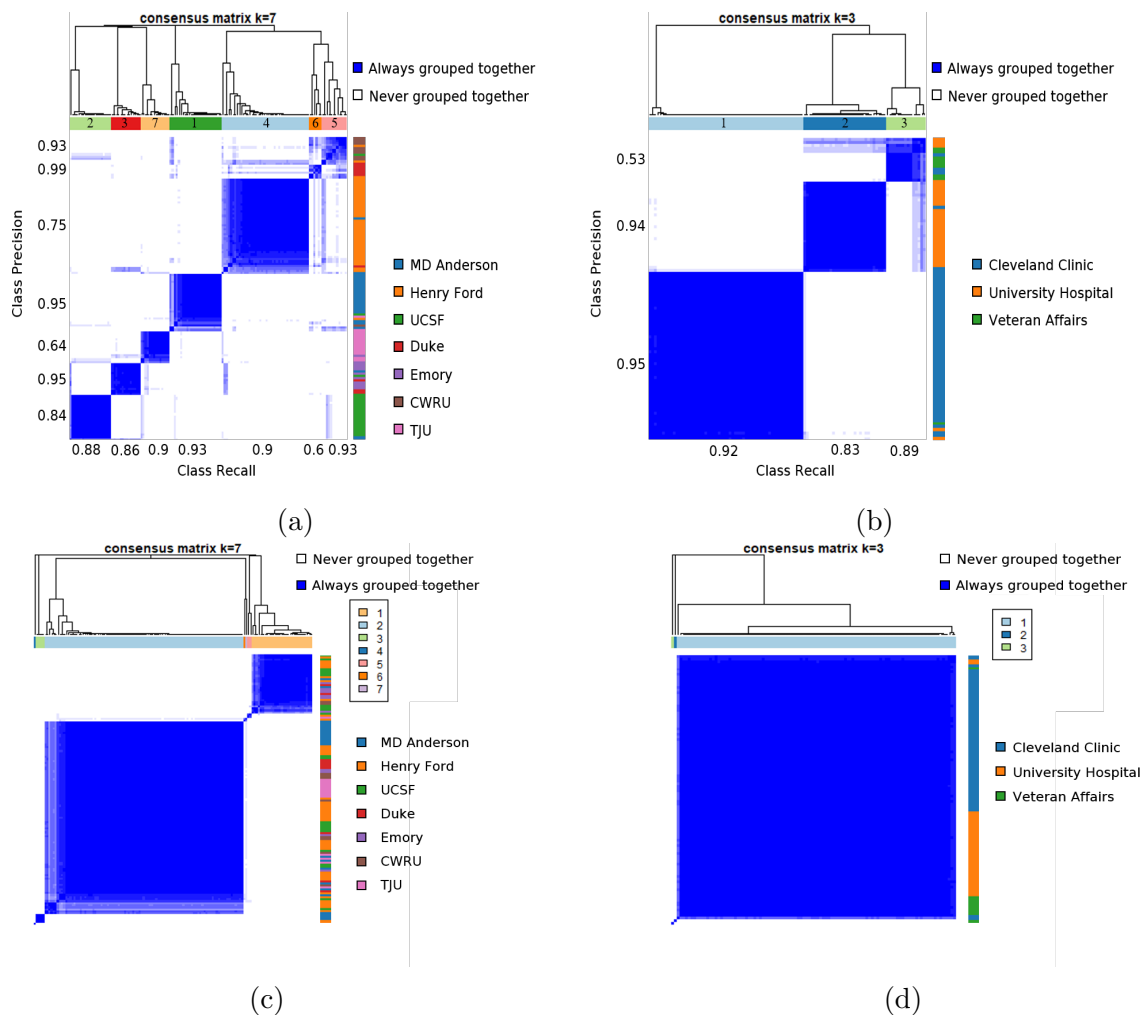


Figure 7: Consensus clustegram of all 23 MRQy measures computed for (a) unprocessed TCGA-GBM cohort, (b) unprocessed rectal cohort, (c) processed TCGA-GBM cohort, and (d) processed rectal cohort. In each plot, the colorbar along the right corresponds indicates which site each dataset belongs to (legend alongside) while the colorbar at the top is the cluster label obtained via consensus clustering. For unprocessed data, precision and recall values for each cluster in identifying a specific site are also noted along the left and bottom of the clustergram, respectively.

## IV. Discussion

We have presented a technical overview and experimental evaluation of a novel open-source quality control tool for MR imaging data; called MRQy. Using cohorts from 2 different body regions (brain MRIs from TCIA, in-house rectal MRIs), we demonstrated that MRQy can quantify and evaluate (a) site- or scanner-specific variations within an MRI cohort, (b)

imaging artifacts that compromise relative image quality of MRI datasets, and (c) how well specific processing pipelines have accounted for artifacts that are present in an given data cohort.

As each of the metadata and quality measures extracted within MRQy can be used to reveal a variety of different artifacts that may be present in MR images, we opted to examine two representative exemplar artifacts in this work. Our results demonstrate that we were able to accurately identify datasets with specific intensity and noise artifacts in this fashion, as they appear as distinct outliers in our specialized interface. More importantly, by iteratively using MRQy to QC the cohorts, we were able to determine how well these artifacts were corrected in the processed MRI datasets (i.e. after artifact correction and image normalization operations were performed). We additionally conducted an extensive qualitative and quantitative evaluation for the presence of batch effects in both cohorts, both before and after processing. While the presence of batch effects and their impact on IQMs have been evaluated in previous studies<sup>18</sup> from a supervised learning perspective, we used a consensus clustering approach to quantify how well specific sites could be identified in the cohort in a completely unsupervised fashion. This provided us a purely data-driven indication of how well the processing pipelines have corrected the site- and scanner-specific variations present in both cohorts considered in this work. While MRQy was used to evaluate MRI datasets processed using specific pipelines, our tool could be used to evaluate the impact of individual steps within the pipeline as thus determine the optimal sequence of processing operations that should be applied to a given MRI cohort.

Quality control of MR imaging has long been a topic of active research<sup>19,20,22,23,44</sup>, but a majority of the resulting tools have been specifically developed for brain MRIs<sup>18,25,26</sup> in order to identify acceptable scans via supervised learning (based on subjective expert quality ratings). By contrast, MRQy represents a unique solution for quality control of MRI datasets that has been designed to work with scans of any body region while running in an efficient and unsupervised fashion. MRQy has been developed by expanding on an initial framework developed as part of a digital pathology quality control tool, HistoQC<sup>27</sup>, but has been evolved significantly to specialize it for MR imaging data by incorporating imaging-specific processing steps and quality measures. Unlike existing approaches for MRI quality control, MRQy also includes a specialized interactive front-end which can help quickly identify what relative imaging artifacts and batch effects are present in a cohort. While the current work has been

limited to demonstrating detection of 2 specific artifacts (shading, noise) via MRQy, we believe this approach will generalize to other artifacts due to the extensive list of extracted quality measures which have been previously validated for this purpose<sup>18</sup>.

The recent focus on the reproducibility of radiomics and deep learning across sites<sup>45</sup> implies a need to interrogate cohort differences which can cause models trained on one site to fail to generalize on another. To enable this, we have released results of our QC analysis of MRI studies from the TCGA-GBM as well as 2 other TCIA collections (<https://doi.org/10.7937/K9/TCIA.2020.JHZ2-T694>) which could help researchers in addressing these questions for large-scale multi-site or multi-scanner cohorts<sup>15,46</sup>. We envision using MRQy as a pre-analytic step in any computational imaging pipeline to determine (a) what site- or scanner-specific variations need to be accounted for to accurately characterize “true” biological differences, as well as (b) which corrections should be applied to curate datasets of acceptable relative quality (i.e. minimal or no outliers); prior to model development or validation.

Further development of MRQy has been enabled by its modular design, exemplified by the HTML front-end which is already highly customizable by the end-user. One of our planned functionalities is to enable real-time generation of the embedding scatter plots directly within the MRQy HTML front-end rather than via the backend. Similarly, the Python backend can be easily modified via plugins to use a different foreground detection algorithm, compute additional quality measures, or even to integrate quality prediction algorithms<sup>44,47</sup> in the future. One of the current limitations of MRQy is that it can only be used for quality control of structural MRI data, but we are working on developing new measures that could allow MRQy to be used to interrogate non-structural MRIs (e.g. diffusion or dynamic contrast-enhanced MRI). Additionally, by modifying the quality measures appropriately, this tool could be eventually be adapted for quality control of any radiographic imaging collection (CT, ultrasound, PET, etc.) that is housed in public repositories such as TCIA.

## V. Conclusions

We have presented a technical overview and experimental evaluation of MRQy, a new quality control tool for MR imaging data. MRQy works by computing actionable quality mea-

surements as well as image metadata from any structural MR sequence of any body region via a Python backend, which can be interrogated via a specialized HTML5 front end. MRQy can be executed completely offline and the entire tool requires only a few commands to run in an unsupervised fashion, as well as being designed to be easily extensible and modular. Our initial results successfully demonstrated how MRQy could be used for (a) quantifying site- and scanner-specific batch effects within large multi-site cohorts of MR imaging data (such as TCIA), (b) identifying relative imaging artifacts within MRI datasets which require correction prior to model development, as well as (c) evaluating how well specific processing pipelines have corrected for these issues in a given data cohort. MRQy has been made publicly accessible as an open-source project through GitHub (<https://github.com/ccipd/MRQy>), and can be downloaded as well as contributed to freely by any end-user.

## Acknowledgements

Research reported in this publication was supported by the National Cancer Institute of the National Institutes of Health under award numbers 1U24CA199374-01, R01CA202752-01A1, R01CA208236-01A1, R01CA216579-01A1, R01CA220581-01A1, 1U01CA239055-01, 1F31CA216935-01A1, 1U01CA248226-01, National Institute for Biomedical Imaging and Bioengineering 1R43EB028736-01, National Center for Research Resources under award number 1 C06 RR12463-01, VA Merit Review Award IBX004121A from the United States Department of Veterans Affairs Biomedical Laboratory Research and Development Service, the DoD Breast Cancer Research Program Breakthrough Level 1 Award (W81XWH-19-1-0668), the DOD Prostate Cancer Idea Development Award (W81XWH-15-1-0558), the DOD Lung Cancer Investigator-Initiated Translational Research Award (W81XWH-18-1-0440), the DOD Peer Reviewed Cancer Research Program (W81XWH-16-1-0329, W81XWH-18-1-0404), the Kidney Precision Medicine Project (KPMP) Glue Grant, the Dana Foundation David Mahoney Neuroimaging Program, the V Foundation Translational Research Award, the Ohio Third Frontier Technology Validation Fund, the Wallace H. Coulter Foundation Program in the Department of Biomedical Engineering and The Clinical and Translational Science Award Program (CTSA) at Case Western Reserve University.

The content is solely the responsibility of the authors and does not necessarily represent

the official views of the National Institutes of Health, the U.S. Department of Veterans Affairs, the Department of Defense, or the United States Government.

# Supplementary Materials

## Definitions

*Batch effects* refer to systematic occurrence of a technical artifact within a subset of a cohort<sup>10</sup>. For example, the slice spacing may be different between two institutions, creating a batch effect if those studies were evaluated in unison. Consider the following example. Site A produces MR volumes with a larger slice spacing as well as a majority of the cases belonging to the positive target class, while Site B provides MR volumes with much smaller slice spacing and a majority of cases from the negative class. When combining data from both sites, any developed model must be optimized to identify biologically relevant features specific to the target class, as opposed to determining that slice spacing may be relevant for distinguishing between the 2 classes (as the latter is really an acquisition difference between the 2 sites).

*Image artifacts* refer to the image quality issues such as the presence of noise, motion, shading, lack of detail, ringing, aliasing or other issues; that are present within individual MR datasets to varying degrees<sup>21</sup>. These typically occur as a result of the acquisition process, scanner calibration issues, or technician error.

## Format and Usage

MRQy has been made publicly accessible as an open-source project through GitHub (<https://github.com/ccipd/MRQy>), and can be downloaded as well as contributed to freely by any end-user. Specific package dependencies for MRQy have included in the GitHub documentation. After the installation of all the prerequisite Python packages (specified in the installation instructions), MRQy can be run on a directory containing files for a given cohort via the command: `python QC.py output_folder_name "input directory address`. No additional configuration files need to be specified. This results in the following steps being executed:

- Thumbnail images are generated for all 2D sections in each MRI dataset and saved as *.png* files within the `UserInterface/Data` folder.
- Each dataset is processed to detect the foreground and background region.
- *Metadata* are extracted from file headers for each dataset. *Measurements* are computed based on the detected foreground region for each dataset.
- Both metadata and measurements are saved for each dataset within a tab-separated file (*results.tsv*) that is stored within the `UserInterface/Data` folder.
- For a given cohort, a single UMAP and a single t-SNE embedding are computed for all the datasets based on the 23 measures (after whitening). The embedding co-ordinates are also saved into the *results.tsv* file.

Further interrogation of cohort variations and artifact trends may be done reading *results.tsv* into any common data analytic tool (e.g. MATLAB or R). A specialized front-end HTML interface (*index.html*) is available within the `UserInterface` folder designed for real-time manipulation and visualization. Quality control can be performed via multiple pathways:

- Using sorting arrows available on each table column to re-order measures and examine numeric trends. Users can further annotate rows or remove non-informative patients.
- As the different interface components are synchronized, if a patient row is highlighted in either Table, a corresponding highlight appears on a line within the PC chart, on a bar in the bar chart, as well as shading the patient-specific bubble in the embedding plots. Thumbnail images for this patient volume are shown in the interface.
- Using the PC and bar charts to directly compare a specific measure across all the subject scans. This can help quickly determine which of the metadata or measures are consistent across the entire cohort as well as identify outliers. The PC chart can also be used to evaluate positive or negative relationships between different measures<sup>43</sup> and thus determine the trade-off in processing for specific artifacts.
- Using embedding plots (t-SNE and UMAP) to track specific site- or scanner-specific trends within the cohort. By visualizing the 2D space into which the entire cohort has been mapped, any clusters that can be identified typically correspond to site- and scanner-specific variations. The overall distribution of points in space also provide an indication of the variability within the entire cohort.

---

## User-Specified Settings

By default, MRQy extracts a basic set of 10 metadata tags from *.dcm* files, summarized in Table 2. Additional tag fields or private metadata can also be extracted by specifying them via a *.txt* file and using the syntax:

```
python QC.py output_folder_name "input directory -t "tags .txt address.
```

The user can also specify a configuration for the foreground detection algorithm using the following command:

```
python QC.py output_folder_name "input directory -c "False.
```

Note that the default value for the `-c` flag is *False*, where MRQy measures are computed across all foreground objects together. When the `-c` flag is *True*, MRQy will identify each foreground object separately and compute a measurement per individual object.

## References

- <sup>1</sup> K. Clark et al., The Cancer Imaging Archive (TCIA): maintaining and operating a public information repository, *Journal of digital imaging* **26**, 1045–1057 (2013).
- <sup>2</sup> F. Prior, K. Smith, A. Sharma, J. Kirby, L. Tarbox, K. Clark, W. Bennett, T. Nolan, and J. Freymann, The public cancer radiology imaging collections of The Cancer Imaging Archive, *Scientific data* **4**, 170124 (2017).
- <sup>3</sup> J. Kalpathy-Cramer, J. B. Freymann, J. S. Kirby, P. E. Kinahan, and F. W. Prior, Quantitative imaging network: data sharing and competitive Algorithm Validation leveraging the cancer imaging archive, *Translational oncology* **7**, 147–152 (2014).
- <sup>4</sup> M. Zanfardino, K. Pane, P. Mirabelli, M. Salvatore, and M. Franzese, TCGA-TCIA Impact on Radiogenomics Cancer Research: A Systematic Review, *International Journal of Molecular Sciences* **20**, 6033 (2019).
- <sup>5</sup> F. Prior, J. Almeida, P. Kathiravelu, T. Kurc, K. Smith, T. Fitzgerald, and J. Saltz,

---

Open access image repositories: high-quality data to enable machine learning research, *Clinical radiology* **75**, 7–12 (2020).

- <sup>6</sup> A. Basu, D. Warzel, A. Eftekhari, J. S. Kirby, J. Freymann, J. Knable, A. Sharma, and P. Jacobs, Call for Data Standardization: Lessons Learned and Recommendations in an Imaging Study, *JCO Clinical Cancer Informatics* **3**, 1–11 (2019).
- <sup>7</sup> C. L. Schlett et al., Quantitative, organ-specific interscanner and intrascanner variability for 3 T whole-body magnetic resonance imaging in a multicenter, multivendor study, *Investigative radiology* **51**, 255–265 (2016).
- <sup>8</sup> B. Glocker, R. Robinson, D. C. Castro, Q. Dou, and E. Konukoglu, Machine learning with multi-site imaging data: An empirical study on the impact of scanner effects, arXiv preprint [arXiv:1910.04597](https://arxiv.org/abs/1910.04597) (2019).
- <sup>9</sup> C. Wachinger, B. G. Becker, A. Rieckmann, and S. Pölsterl, Quantifying confounding bias in neuroimaging datasets with causal inference, in *International Conference on Medical Image Computing and Computer-Assisted Intervention*, pages 484–492, Springer, 2019.
- <sup>10</sup> J. T. Leek, R. B. Scharpf, H. C. Bravo, D. Simcha, B. Langmead, W. E. Johnson, D. Geman, K. Baggerly, and R. A. Irizarry, Tackling the widespread and critical impact of batch effects in high-throughput data, *Nature Reviews Genetics* **11**, 733–739 (2010).
- <sup>11</sup> L. Scarpace, T. Mikkelsen, S. Cha, S. Rao, S. Tekchandani, D. Gutman, J. Saltz, B. Erickson, N. Pedano, A. Flanders, J. Barnholtz-Sloan, Q. Ostrom, D. Barboriak, and L. Pierce, Radiology Data from The Cancer Genome Atlas Glioblastoma Multiforme [TCGA-GBM] collection, The Cancer Imaging Archive , <http://doi.org/10.7937/K9/TCIA.2016.RNYFUYE9>.
- <sup>12</sup> A. Zwanenburg et al., The Image Biomarker Standardization Initiative: standardized quantitative radiomics for high-throughput image-based phenotyping, *Radiology*, 191145 (2020).
- <sup>13</sup> L. Erasmus, D. Hurter, M. Naudé, H. Kritzinger, and S. Acho, A short overview of MRI artefacts, *SA Journal of Radiology* **8** (2004).



- 
- <sup>14</sup> J. T. Bushberg, J. A. Seibert, E. M. Leidholdt, and J. M. Boone, *The essential physics of medical imaging*, Lippincott Williams & Wilkins, 2011.
- <sup>15</sup> H. Um, F. Tixier, D. Bermudez, J. O. Deasy, R. J. Young, and H. Veeraraghavan, Impact of image preprocessing on the scanner dependence of multi-parametric MRI radiomic features and covariate shift in multi-institutional glioblastoma datasets, *Physics in Medicine & Biology* **64**, 165011 (2019).
- <sup>16</sup> M. Schwier, J. van Griethuysen, M. G. Vangel, S. Pieper, S. Peled, C. Tempany, H. J. Aerts, R. Kikinis, F. M. Fennessy, and A. Fedorov, Repeatability of multiparametric prostate MRI radiomics features, *Scientific reports* **9**, 1–16 (2019).
- <sup>17</sup> E. A. Gardner, J. H. Ellis, R. J. Hyde, A. M. Aisen, D. J. Quint, and P. L. Carson, Detection of degradation of magnetic resonance (MR) images: comparison of an automated MR image-quality analysis system with trained human observers, *Academic Radiology* **2**, 277–281 (1995).
- <sup>18</sup> O. Esteban, D. Birman, M. Schaer, O. O. Koyejo, R. A. Poldrack, and K. J. Gorgolewski, MRIQC: Advancing the automatic prediction of image quality in MRI from unseen sites, *PloS one* **12** (2017).
- <sup>19</sup> O. Ieremeiev, V. Lukin, N. Ponomarenko, and K. Egiazarian, Robust linearized combined metrics of image visual quality, *Electronic Imaging* **2018**, 260–1–260–6 (2018).
- <sup>20</sup> J. P. Woodard and M. P. Carley-Spencer, No-reference image quality metrics for structural MRI, *Neuroinformatics* **4**, 243–262 (2006).
- <sup>21</sup> D. C. Van Essen et al., The Human Connectome Project: A data acquisition perspective, *NeuroImage* **62**, 2222–2231 (2012).
- <sup>22</sup> B. Mortamet, M. A. Bernstein, C. R. Jack, J. L. Gunter, C. Ward, P. J. Britson, R. Meuli, J. P. Thiran, and G. Krueger, Automatic quality assessment in structural brain magnetic resonance imaging, *Magnetic Resonance in Medicine* **62**, 365–372 (2009).
- <sup>23</sup> R. A. Pizarro, X. Cheng, A. Barnett, H. Lemaitre, B. A. Verchinski, A. L. Goldman, E. Xiao, Q. Luo, K. F. Berman, J. H. Callicott, D. R. Weinberger, and V. S. Mattay,
-

---

Automated quality assessment of structural magnetic resonance brain images based on a supervised machine learning algorithm, *Frontiers in Neuroinformatics* **10** (2016).

- <sup>24</sup> O. Esteban, R. W. Blair, D. M. Nielson, J. C. Varada, S. Marrett, A. G. Thomas, R. A. Poldrack, and K. J. Gorgolewski, Crowdsourced MRI quality metrics and expert quality annotations for training of humans and machines, *Scientific data* **6**, 1–7 (2019).
- <sup>25</sup> E. T. Klapwijk, F. van de Kamp, M. van der Meulen, S. Peters, and L. M. Wierenga, Qoala-T: A supervised-learning tool for quality control of FreeSurfer segmented MRI data, *NeuroImage* **189**, 116 – 129 (2019).
- <sup>26</sup> C. Vogelbacher, M. H. Bopp, V. Schuster, P. Herholz, A. Jansen, and J. Sommer, LAB-QA2GO: A free, easy-to-use toolbox for the quality assessment of magnetic resonance imaging data, *Frontiers in neuroscience* **13**, 688 (2019).
- <sup>27</sup> A. Janowczyk, R. Zuo, H. Gilmore, M. Feldman, and A. Madabhushi, HistoQC: an open-source quality control tool for digital pathology slides, *JCO clinical cancer informatics* **3**, 1–7 (2019).
- <sup>28</sup> P. S. Foundation, The Python Package Index (PyPI), <https://pypi.org/>.
- <sup>29</sup> Y. Feng, H. Zhao, X. Li, X. Zhang, and H. Li, A multi-scale 3D Otsu thresholding algorithm for medical image segmentation, *Digital Signal Processing* **60**, 186 – 199 (2017).
- <sup>30</sup> S. Navdeep, K. Lakhwinder, and S. Kuldeep, Histogram equalization techniques for enhancement of low radiance retinal images for early detection of diabetic retinopathy, *Engineering Science and Technology* **22**, 736 – 745 (2019).
- <sup>31</sup> S. van der Walt, J. L. Schönberger, J. Nunez-Iglesias, F. Boulogne, J. D. Warner, N. Yager, E. Gouillart, T. Yu, and the scikit-image contributors, scikit-image: image processing in Python, *PeerJ* **2**, e453 (2014).
- <sup>32</sup> S. Hui, T. Zhang, L. Shi, D. Wang, C. Ip, and W. Chu, Automated segmentation of abdominal subcutaneous adipose tissue and visceral adipose tissue in obese adolescent in MRI, *Magnetic Resonance Imaging* **45**, 97 – 104 (2018).

- 
- <sup>33</sup> B. Mnahi, A. Faisal, F. Faisal, A. Khalefa, P. Nadeem, and S. Ghosh, Check the chest: review of chest findings on abdominal MRI, *Clinical Imaging* **59**, 68 – 77 (2020).
- <sup>34</sup> S. Z. K. Sajib, N. Katoch, H. J. Kim, O. I. Kwon, and E. J. Woo, Software Tool-box for Low-Frequency Conductivity and Current Density Imaging Using MRI, *IEEE Transactions on Biomedical Engineering* **64**, 2505 – 2514 (2017).
- <sup>35</sup> S.-J. Chang, S. Li, A. Andreassen, X.-Z. Sha, and X.-Y. Zhai, A reference-free method for brightness compensation and contrast enhancement of micrographs of serial sections, *PloS one* **10** (2015).
- <sup>36</sup> O. Dietrich, J. G. Raya, S. B. Reeder, M. F. Reiser, and S. O. Schoenberg, Measurement of signal-to-noise ratios in MR images: influence of multichannel coils, parallel imaging, and reconstruction filters, *Journal of Magnetic Resonance Imaging: An Official Journal of the International Society for Magnetic Resonance in Medicine* **26**, 375–385 (2007).
- <sup>37</sup> R. M. Edsall, The parallel coordinate plot in action: design and use for geographic visualization, *Computational Statistics & Data Analysis* **43**, 605–619 (2003).
- <sup>38</sup> L. v. d. Maaten and G. Hinton, Visualizing data using t-SNE, *Journal of machine learning research* **9**, 2579–2605 (2008).
- <sup>39</sup> L. McInnes, J. Healy, and J. Melville, Umap: Uniform manifold approximation and projection for dimension reduction, *arXiv preprint [arXiv:1802.03426](https://arxiv.org/abs/1802.03426)* (2018).
- <sup>40</sup> S. Bakas, H. Akbari, A. Sotiras, M. Bilello, M. Rozycki, J. S. Kirby, J. B. Freymann, K. Farahani, and C. Davatzikos, Advancing the cancer genome atlas glioma MRI collections with expert segmentation labels and radiomic features, *Scientific data* **4**, 170117 (2017).
- <sup>41</sup> C. Hui, Y. X. Zhou, and P. Narayana, Fast algorithm for calculation of inhomogeneity gradient in magnetic resonance imaging data, *Journal of Magnetic Resonance Imaging* **32**, 1197–1208 (2010).
- <sup>42</sup> J. T. Antunes, A. Ofshteyn, K. Bera, E. Y. Wang, J. T. Brady, J. E. Willis, K. A. Friedman, E. L. Marderstein, M. F. Kalady, S. L. Stein, A. S. Purysko, R. Paspulati, J. Gollamudi, A. Madabhushi, and S. E. Viswanath, Radiomic Features of Primary

---

Rectal Cancers on Baseline T2-Weighted MRI Are Associated With Pathologic Complete Response to Neoadjuvant Chemoradiation: A Multisite Study, *Journal of Magnetic Resonance Imaging* **n/a**.

- <sup>43</sup> A. Inselberg, Multidimensional detective, in *Proceedings of VIZ '97: Visualization Conference, Information Visualization Symposium and Parallel Rendering Symposium*, pages 100–107, 1997.
- <sup>44</sup> Y. Ding, S. Suffren, P. Bellec, and G. A. Lodygensky, Supervised machine learning quality control for magnetic resonance artifacts in neonatal data sets, *Human brain mapping* **40**, 1290–1297 (2019).
- <sup>45</sup> P. Chirra, P. Leo, M. Yim, B. N. Bloch, A. R. Rastinehad, A. Purysko, M. Rosen, A. Madabhushi, and S. E. Viswanath, Multisite evaluation of radiomic feature reproducibility and discriminability for identifying peripheral zone prostate tumors on MRI, *Journal of Medical Imaging* **6**, 024502 (2019).
- <sup>46</sup> H. Moradmand, S. M. R. Aghamir, and R. Ghaderi, Impact of image preprocessing methods on reproducibility of radiomic features in multimodal magnetic resonance imaging in glioblastoma, *Journal of Applied Clinical Medical Physics* (2019).
- <sup>47</sup> M. E. Osadebey et al., Standardized quality metric system for structural brain magnetic resonance images in multi-center neuroimaging study, *BMC medical imaging* **18**, 31 (2018).
- <sup>48</sup> Y. Wang, Y. Zhang, W. Xuan, E. Kao, P. Cao, B. Tian, K. Ordovas, D. Saloner, and J. Liu, Fully automatic segmentation of 4D MRI for cardiac functional measurements, *Medical Physics* **46**, 180–189 (2019).
- <sup>49</sup> D. Sage and M. Unser, Teaching Image-Processing Programming in Java, *IEEE Signal Processing Magazine* **20**, 43–52 (2003).
- <sup>50</sup> Z. Shehzad, S. Giavasis, Q. Li, Y. Benhajali, C. Yan, Z. Yang, M. Milham, P. Bellec, and C. Craddock, The Preprocessed Connectomes Project Quality Assessment Protocols resource for measuring the quality of MRI data, *Frontiers in neuroscience* **47** (2015).

- 
- <sup>51</sup> S. Monti, P. Tamayo, J. Mesirov, and T. Golub, Consensus clustering: a resampling-based method for class discovery and visualization of gene expression microarray data, *Machine learning* **52**, 91–118 (2003).
- <sup>52</sup> M. D. Wilkerson and D. N. Hayes, ConsensusClusterPlus: a class discovery tool with confidence assessments and item tracking, *Bioinformatics* **26**, 1572–1573 (2010).
- <sup>53</sup> N. Beig, K. Bera, P. Prasanna, J. Antunes, R. Correa, S. Singh, A. Saeed Bamashmos, M. Ismail, N. Braman, R. Verma, V. B. Hill, V. Statsevych, M. S. Ahluwalia, V. Varadan, A. Madabhushi, and P. Tiwari, Radiogenomic-based survival risk stratification of tumor habitat on Gd-T1w MRI is associated with biological processes in Glioblastoma, *Clinical Cancer Research* **26** 1866–1876 (2020).
- <sup>54</sup> T. Rohlfing, N. M. Zahr, E. V. Sullivan, and A. Pfefferbaum, The SRI24 multichannel atlas of normal adult human brain structure, *Human brain mapping* **31**, 798–819 (2010).
- <sup>55</sup> A. Keshavan, E. Datta, I. McDonough, C. Madan, K. Jordan, and R. Henry, Mindcontrol: A web application for brain segmentation quality control, *NeuroImage* **170**, 365–372 (2018).
- <sup>56</sup> P.R. Raamana, Mindcontrol: VisualQC: Assistive tools for easy and rigorous quality control of neuroimaging data, (2018).
- <sup>57</sup> C. Davatzikos et al., Cancer imaging phenomics toolkit: quantitative imaging analytics for precision diagnostics and predictive modeling of clinical outcome, *Journal of medical imaging* **5**, 011018 (2018).
- <sup>58</sup> S. M. Smith and J. M. Brady, SUSAN: a new approach to low level image processing, *International journal of computer vision* **23**, 45–78 (1997).
- <sup>59</sup> N. J. Tustison, B. B. Avants, P. A. Cook, Y. Zheng, A. Egan, P. A. Yushkevich, and J. C. Gee, N4ITK: improved N3 bias correction, *IEEE transactions on medical imaging* **29**, 1310–1320 (2010).
- <sup>60</sup> M. R. S. Sunoqrot, G. A. Nketiah, K. M. Selnaes, T. F Bathen, and M. Elschot, Automated reference tissue normalization of T2-weighted MR images of the prostate using

---

object recognition, *Magnetic Resonance Materials in Physics, Biology and Medicine* 1–13 (2020).

- <sup>61</sup> L. G. Nyul, J. K. Udupa, and X. Zhang, New variants of a method of MRI scale standardization, *IEEE transactions on medical imaging* **19**, 143–150 (2000).
- <sup>62</sup> E. Scalco, A. Belfatto, A. Mastropietro, T. Rancati, B. Avuzzi, A. Messina, R. Valdagni, and G. Rizzo, T2w-MRI signal normalization affects radiomics features reproducibility, *Medical Physics* **47**, 1680–1691 (2020).
- <sup>63</sup> H. Delis, K. Christaki, B. Healy, G. Loreti, G. L. Poli, P. Toroi, and A. Meghzifene, Moving beyond quality control in diagnostic radiology and the role of the clinically qualified medical physicist, *Physica Medica* **41**, 104–108 (2017).
- <sup>64</sup> S. Ondategui-Parra, Quality Management in Radiology: Defining the Parameters, *Health Management* **8(4)**, (2008).